

Fast XANES fluorescence imaging using a Maia detector

Ulrike Boesenberg,^{a,b,*} Christopher G. Ryan,^c Robin Kirkham,^c Andreas Jahn,^d Anders Madsen,^a Gareth Moorhead,^c Gerald Falkenberg^b and Jan Garrevøet^b

^aEuropean X-ray Free-Electron Laser Facility, Holzkoppel 4, Schenefeld 22869, Germany, ^bDeutsches Elektronen-Synchrotron DESY, Notkestrasse 85, Hamburg 22607, Germany, ^cCommonwealth Scientific and Industrial Research Organisation (CSIRO), Clayton, Victoria, Australia, and ^dInstitut für Halbleiter- und Mikrosystemtechnik, Technische Universität Dresden, Dresden 01062, Germany. *Correspondence e-mail: ulrike.boesenberg@xfel.eu

Received 15 August 2017

Accepted 27 March 2018

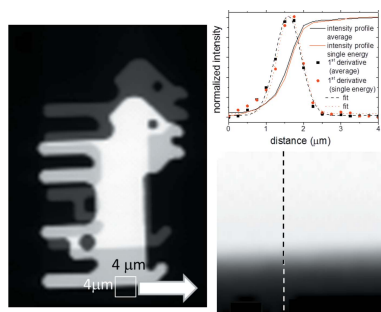
Edited by I. Schlichting, Max Planck Institute for Medical Research, Germany

Keywords: QXANES; Maia detector; micro-XRF; spectromicroscopy.

A new fast X-ray absorption spectroscopy scanning method was recently implemented at the Hard X-ray Microprobe endstation P06, PETRA III, DESY, utilizing a Maia detector. Spectromicroscopy maps were acquired with spectra for X-ray absorption near-edge structure (XANES) acquisition in the sub-second regime. The method combines XANES measurements with raster-scanning of the sample through the focused beam. The order of the scanning sequence of the axes, one beam energy axis and two (or more) spatial axes, is a variable experimental parameter and, depending on it, the dwell at each location can be either single and continuous (if the energy axis is the inner loop) or in shorter discontinuous intervals (if a spatial axis is innermost). The combination of improved spatial and temporal resolution may be necessary for rapidly changing samples, *e.g.* for following *in operando* chemical reactions or samples highly susceptible to beam damage where the rapid collection of single XANES spectra avoids issues with the emergence of chemical changes developing from latent damage. This paper compares data sets collected on a specially designed test pattern and a geological thin-section scanning the energy as inner, middle and outer axis in the sequence. The XANES data of all three scanning schemes is found to show excellent agreement down to the single-pixel level.

1. Introduction

Spectromicroscopy through collection of sets of two-dimensional images in the direct vicinity of an X-ray absorption edge has become a common technique with the advancement of third-generation synchrotron sources and detector technology. The datasets with two (or three) spatial axes and one incident beam energy axis provide information about the spatial distribution of a chemical species and permit deep insights into chemical processes in a range of scientific fields including biology, materials science, catalysis, geology and cultural heritage (Meirer *et al.*, 2011; de Jonge *et al.*, 2014; Monico *et al.*, 2015). Depending on the detection system, datasets can be collected in either full-field mode using two-dimensional detectors with spatial resolution, or in a scanned sample mode using a focused micro-beam and a detector without spatial resolution. The scanning approach provides the opportunity to choose the order of the scan axes, that is, whether the measurement proceeds as a series of maps acquired as the incident beam energy is slowly varied across an absorption edge or as a series of spectra that are acquired serially at each location across the specimen. Due to time restrictions, larger spectromicroscopy maps are often limited to a rather small energy range around an absorption edge (*e.g.* <150 eV), the



so-called X-ray absorption near-edge structure (XANES), but can be complemented by extended X-ray absorption fine-structure (EXAFS) measurements at selected points of interest to provide more details on the chemical species present.

Of the three axes in such scans, the photon energy is typically the ‘outer loop’, the slowest axis in the scan sequence. This is because in most micro-focus beamlines the monochromator motion control systems are optimized for stability rather than speed, and also because energy scanning over a larger range often requires coordinated movement of insertion devices and the monochromator. On the other hand, dedicated quick-scanning EXAFS (QEXAFS) instruments can provide extremely high scanning speeds, *e.g.* to follow chemical reactions *in operando*, but typically such instruments lack spatial resolution. However, in certain cases high-spatial-resolution chemical information is required in combination with good temporal resolution. Examples are microscopic *in operando* experiments, or those with radiation-sensitive or otherwise rapidly changing heterogeneous samples. In these cases, scanning with the energy as the outer axis leads to distorted spectra, either due to chemical or spatial shifts. Using an energy-dispersive fluorescence detector the lower detection limits for emission-based XANES spectroscopy in comparison with transmission-based measurements enable the measurement of low-concentration and diluted samples. Furthermore, additional information on other elements in the sample that have an electron binding energy below the incident energy is collected, which can provide excellent spatial context for the spectroscopy element of interest.

QEXAFS was first described in the early 1990s for improved time-dependent studies such as *in situ* following of chemical reactions (Prieto *et al.*, 1992; Frahm, 1988, 1989; Als-Nielsen *et al.*, 1995; Khalid *et al.*, 2010). Recently a number of synchrotron beamlines around the world have been equipped with dedicated monochromators for highest temporal resolution (Prestipino *et al.*, 2011; Mathon *et al.*, 2015; Müller *et al.*, 2016; Poswal *et al.*, 2016). Typically, for scanning rates at multiple Hertz (up to 100 EXAFS spectra per second), samples are concentrated and the beam is relatively large to acquire statistically significant signal. With these oscillating monochromator designs, channel-cut crystals are favored for their robustness but they do not provide a fixed beam position on the sample when changing the energy and thus do not allow spatially resolved measurements.

In contrast to dedicated QEXAFS instruments, the setup described here uses an existing micro-focus beamline. We compromise the temporal resolution, with about 1 Hz scanning in the XANES region (depending on the concentration levels in the samples) and about 30 s per scan for a full high-resolution EXAFS scan (Chernikov *et al.*, 2016). Improvements were made to the technical implementation of the hardware readout of the energy (monochromator Bragg axis position) during continuous scanning in order to correlate transmission and emission signals and photon energy precisely. Furthermore, detectors and detector electronics capable of acquisition times in the millisecond range are

necessary to provide sufficient spectral resolution. The Maia detector fulfills these requirements (Ryan *et al.*, 2010, 2014; Kirkham *et al.*, 2010; Siddons *et al.*, 2014) particularly given its capability to directly read-in the encoder outputs of the scanning axes, and for scanning to occur in any sequence (Kirkham *et al.*, 2010).

In the present paper we report on a comparison of spectromicroscopy measurements taken at different scan sequences of spatial and energy axes. The experiments were conducted in fluorescence mode with a sub-micrometer focused beam scanning the sample in two dimensions using a Maia detector at the P06 beamline, PETRA III, Deutsches Elektronen-Synchrotron (DESY), Germany (Boesenberg *et al.*, 2016). The set-up was characterized with a specially designed Ta/Ta₂O₅ test pattern and a geological thin section, directly comparing conventional measurements with the energy as the outer axis with fast XANES results with the energy as the inner scanned axis. Additionally we collected a data set with the energy axis as the middle axis in the sequence. All methods show excellent agreement down to single-pixel level in both the spatial distribution of the chemical phases as well as with single-pixel XANES spectra; their advantages and disadvantages are discussed.

2. Experimental

The measurements were performed at the canted undulator beamline P06 of the third-generation light source PETRA III, DESY, Germany (Schroer *et al.*, 2005). The beamline combines a 2 m spectroscopy undulator with a period length of 31.4 mm with a cryogenically cooled fixed-exit Si 111 double-crystal monochromator (DCM) or Si 111 channel-cut crystal with an energy resolution of approximately $\Delta E/E \simeq 1.4 \times 10^{-4}$, manufactured by FMB Oxford. Special control routines were implemented to ensure coordinated motion of monochromator (master) and undulator (slave), similar to the experiments described by Chernikov *et al.* (2016). The aim is to synchronize the continuous Bragg axis movement of the monochromator with the undulator gap scan in order to match the photon energies. The task is complicated by a nonlinear relation between the motor and energy axes. The control routine includes therefore a feedback loop which reads the positions of the motors defining the Bragg angle (monochromator energy) and undulator gap from the corresponding encoders, estimates the misalignment and regulates the motor movement of the undulator gap to a maximum deviation of the photon energy of the Bragg axis of 1 eV.

The Maia detector uses an event-by-event data acquisition and imaging scheme for energy-dispersive detection allowing a dwell time per image pixel as low as 50 μ s, and photon rates higher than $2 \times 10^7 \text{ s}^{-1}$ (Kirkham *et al.*, 2010; Ryan *et al.*, 2010, 2014). The general setup with the Maia detector mounted in backscattering geometry at the microfocus endstation of the P06 beamline is described in detail elsewhere (Boesenberg *et al.*, 2016). A schematic of the setup at the beamline is shown in Fig. 1. An achromatic optic, fixed curvature Kirkpatrick–Baez (KB) mirrors, was used to focus the beam to about $0.5 \mu\text{m} \times$

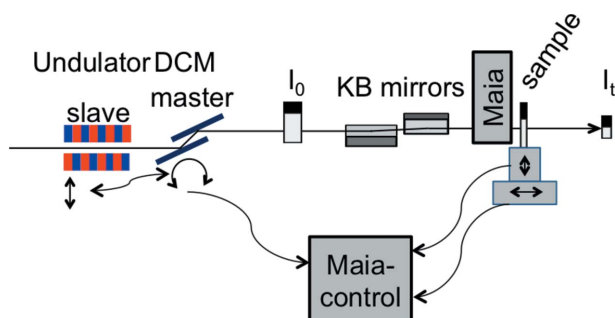


Figure 1
Schematic setup at the P06 beamline, PETRA III, DESY, for the fast energy scanning.

0.5 μm , or larger. The sample was then raster scanned in two image dimensions with each image pixel $1 \mu\text{m} \times 1 \mu\text{m}$ in size and the energy scanned with continuous motion of the monochromator Bragg axis combined with the undulator gap motion. The monochromator Bragg axis incremental encoder signal was fed directly into Maia controller hardware in the same way as those tracking sample motion. Emission data were acquired during both low-to-high and high-to-low energy moves. The Bragg axis was subdivided into intervals using the Maia's spatial pixilation mechanism driven by the encoder signal from the Bragg axis, and in each interval all detected photon events were recorded and tagged by a pixel address, which contains the spatial and energy values. The analysis software *GeoPIXE* (Ryan *et al.*, 2015) was adapted to analyze the acquired three-dimensional data cube event-by-event taking into account the non-linear changes of incident energy with respect to the linear motion of the Bragg axis. The dynamic analysis (DA) method (Ryan *et al.*, 1990), implemented in *GeoPIXE*, uses a set of DA matrices that span the scanned energy range which are used to deconvolute the photon spectrum to elemental emission intensity. For each Bragg interval $\Delta\theta$ during the continuous scan, the incident energy was calculated and the appropriate DA matrix was selected automatically. This resulted in a data cube of two-dimensional spatial maps varying in the incident energy for the respective element around the absorption edge. Further analysis to extract the single-pixel XANES or EXAFS spectrum, and linear combination fitting with measured standards to obtain a two-dimensional distribution of chemical phase maps, was performed using the *TXM-Wizard* software (Liu, Meirer, Williams *et al.*, 2012; Liu, Meirer, Wang *et al.*, 2012). According to the fraction of the two components in each pixel, as determined by linear combination fitting of the appropriate standards, a color-coded chemical phase map was derived.

A specially designed test pattern was used for the characterization of the setup for two-dimensional XANES maps. The pattern was produced by first sputtering a layer of 50 nm metallic tantalum on a silicon substrate using a special mask, then the same mask was shifted by $12 \mu\text{m}$ before applying a second layer of 50 nm of tantalum oxide (Ta_2O_5). An overview of the Ta/ Ta_2O_5 test pattern is shown in Fig. 2. The small region of interest marked by the white box was selected for the direct comparison of the scanning schemes. The distinct

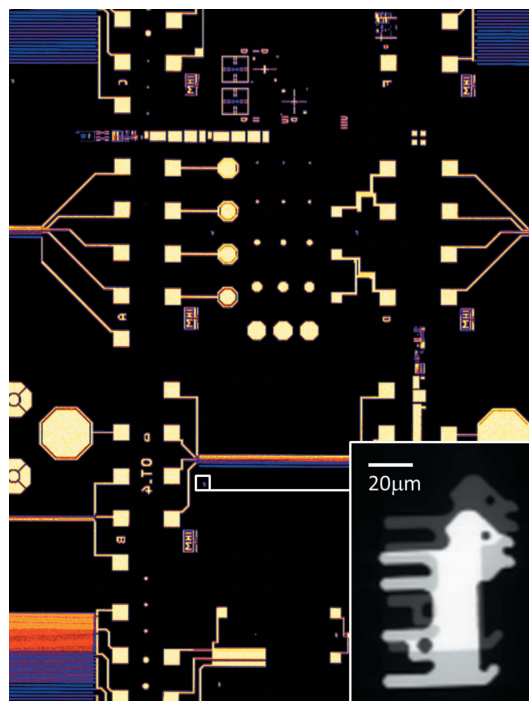


Figure 2
Ta *L* line X-ray fluorescence intensity map providing an overview of the Ta/ Ta_2O_5 test pattern. The inset shows the selected region of interest ('dog') for the further measurements.

features of the object facilitated direct comparison at the single pixel level. Varying the scanning sequence of the spatial and energy axes the test sample was scanned across the Ta *L*III-edge (energy range from 9860 to 9980 eV), with a dwell time of 10 ms per Bragg interval $\Delta\theta$, which corresponded to an energy interval of 0.5 eV at most. A second sample, a geological thin-section, was scanned across the As *K*-edge (11830 to 11920 eV), with a dwell time of 1 ms per Bragg interval $\Delta\theta$, also corresponding to at most 0.5 eV. For both samples data were acquired also in conventional energy stack scan sequences using comparable energy intervals (0.5 eV) across the absorption edges, energy range and dwell time.

3. Results and discussion

The versatility of the setup allows simple switching between two-dimensional mapping at a fixed incident energy and fast XANES scanning, without any hardware modification. Thus, the region of interest can be located from fast overview scans and then immediately scanned using any one of the described scanning sequences. The measurement times required for the different sequences with the same number of energy points, dwell time, number of pixels and pixel size showed only minimal variation for the small ranges scanned in this example. However, it should be noted that the number of energy points can be significantly reduced (by about a factor of two or more) when scanning the energy as the middle or outer axis because probing in the pre- and post-edge can be sparser without loss of information. This was not possible

when scanning the energy as the inner axis as the angular velocity of the Bragg axis was constant.

One critical aspect for the quality of the data cube is spatial consistency, so that exactly the same sample volume is always probed independent of the order of the scanning axes. Using a channel-cut monochromator crystal, this may not be strictly achievable. The shift in beam exit due to the Bragg axis rotation is expected to be 0.011 mm over the energy range probed in the described XANES measurements. However, due to the KB demagnification the focus moves about 300 times less, *i.e.* about 30 nm. With a DCM, correction of the beam position is achieved by altering the position of the second crystal to effectively obtain a fixed-exit operated monochromator. The imperfect movement of the second crystal along the parallel and perpendicular axes to the crystal surface may introduce a misalignment between first and second monochromator crystal, which can lead to a shift of the beam on the sample/focusing optics, *i.e.* a ‘pointing error’, and therefore a drop in photon intensity. Therefore an active feedback system needs to be introduced to correct for the imperfect movement in the parallel and perpendicular direction by altering the pitch of the second monochromator crystal, which is critical since accurate measurements of the photon beam position at high frequencies is challenging.

For the Ta sample scans we used the Si 111 channel-cut monochromator over a range of 140 eV and with beam size of approximately $0.9 \mu\text{m} \times 0.9 \mu\text{m}$. From the overview in Fig. 3(a) collected at a single incident photon energy of 9990 eV we selected a $4 \mu\text{m} \times 4 \mu\text{m}$ region of interest with a horizontal tantalum edge (white box) which was scanned in high-resolution mode with 250 nm sampling interval. This is displayed in Fig. 3(b) with the average Ta concentration from the maps collected above the Ta LIII-edge in the selected region, thus smearing is expected if the beam position varies with the energy. The corresponding intensity profile [marked by the dashed line in Fig. 3(b), black line] is shown in Fig. 3(c) together with its first derivative (black symbols) and the corresponding Gaussian fit (black dashed line) as an indication of the beam size (FWHM $\approx 0.8 \mu\text{m}$). A profile, derivative and fit is shown for a single energy (9900 eV) in Fig. 3(c) in red. As expected, we did not observe a difference between a profile at a single energy and the average, thus no effective beam shift between energies was determined for this beam size, which is in agreement with our initial measurements using a gold wire (not shown).

The Ta fluorescence intensity measured in the three different scanning sequences with the energy as the inner, middle or outer axis is shown in Figs. 4(a), 4(b) and 4(c), respectively, for the same region of interest on the test pattern. Figs. 4(d), 4(e) and 4(f) show the corresponding chemical phase maps after linear combination fitting of each

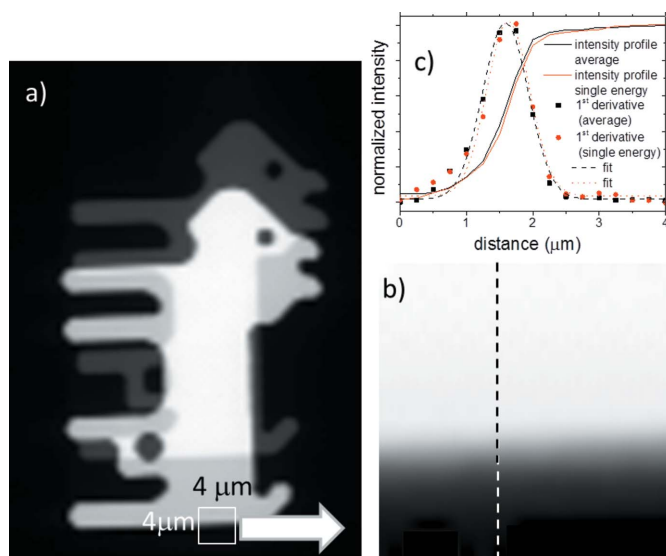


Figure 3

(a) Ta *L*-line X-ray fluorescence map of the selected region of interest collected at 9990 eV incident photon energy. (b) Detail of (a) with a horizontal edge of the Ta pattern with averaged intensity of all maps collected above the Ta *L*-edge as marked in (a) by the white box. (c) Line plot as marked in (b) of the averaged data (black) and a line plot of a single energy (9900 eV, red) and the corresponding first derivatives and fits of a Gaussian beam profile demonstrating the spatial resolution of the measurement.

single-pixel XANES to the standards of Ta in metallic Ta (red) and Ta in Ta₂O₅ (green), a 50:50 mixture of the two components would thus be colored in blue. Since both layers, Ta and Ta₂O₅, have the same thickness of 50 nm, the areal density of Ta atoms in the oxide layer is in practice significantly lower. The gravimetric density of metallic Ta is approximately twice that of Ta₂O₅, which explains the weaker emission intensity observed in this region. This also explains the violet color of the overlaying regions (and point B in Fig. 5) because the relative concentration of Ta atoms in metallic state is higher than the concentration of Ta atoms in Ta₂O₅ coordination. The transparency of the color in the chemical speciation maps

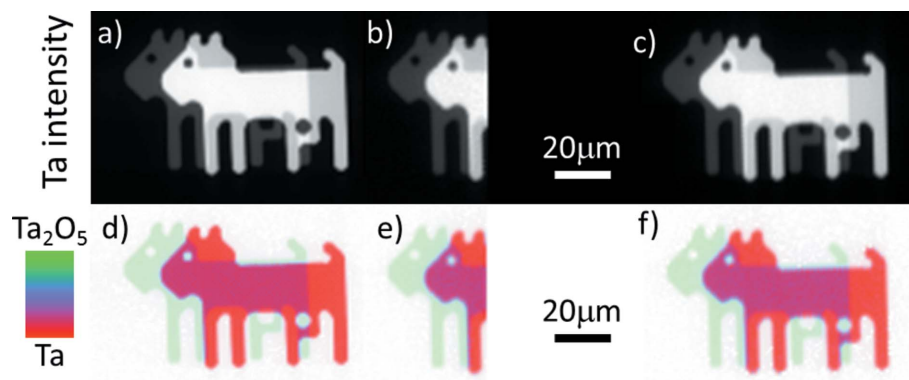


Figure 4

(a)–(c) Ta intensity map of the selected region of interest on the test pattern with the three different scanning sequences of the energy axis. (a) Energy as the inner axis, (b) energy as the middle axis, (c) energy as the outer axis. (d)–(f) Corresponding chemical phase map after linear combination fitting of the single-pixel XANES with metallic Ta (red) and Ta₂O₅ (green).

scales with the intensity of the fluorescence signal and thus the concentration of the respective element, therefore the Ta₂O₅ appears as pale green.

Scanning the energy as the inner axis (Fig. 4a) resulted in a sharper image in comparison with scanning the energy in the middle or outer axis due to a superior horizontal and vertical position stability during the short time period of a single XANES spectrum acquisition.

Fig. 5(a) shows three regions of different Ta concentration in the test pattern. For one selected pixel in each of the points marked in Fig. 5(a) single-pixel XANES are compared for the three different scanning sequences, see Fig. 5(b). Point A corresponds to Ta₂O₅ only, point B to the overlay of Ta₂O₅ and metallic Ta and point C to metallic Ta only. Single-pixel XANES with 10 ms acquisition time for each 0.5 eV energy range was of high and equal quality independent of the order of the scanning axis. The agreement of the single-pixel XANES spectra between all scanning sequences is excellent.

For each scanning sequence with the energy as the first, second and third scanning axis and for each of the selected points A, B and C a single-pixel XANES spectra were extracted (see Fig. 5b) and fit by a linear combination of Ta and Ta₂O₅ reference spectra. This is summarized in Table 1. The given error corresponds to the quality of the fit. For all three scanning schemes variation in the chemical fraction was

Table 1

Linear combination fitting of Ta and Ta₂O₅ components to selected single-pixel XANES for all three measurement schemes; all values are in percent.

Point		Energy = 1st axis	Energy = 2nd axis	Energy = 3rd axis
A	Ta	15.2 ± 0.9%	11.4 ± 0.8%	12.5 ± 1.8%
	Ta ₂ O ₅	84.8 ± 0.9%	88.6 ± 0.9%	87.5 ± 1.8%
B	Ta	74.9 ± 0.6%	76.0 ± 0.7%	78.1 ± 0.8%
	Ta ₂ O ₅	25.1 ± 0.6%	24.0 ± 0.8%	21.9 ± 0.8%
C	Ta	95.2 ± 0.5%	99.7 ± 0.8%	96.0 ± 0.6%
	Ta ₂ O ₅	4.8 ± 0.5%	0.3 ± 0.9%	4.0 ± 0.6%

low with a maximum of 5%. The fraction of Ta as in Ta₂O₅ is less than 100%, although there should be only Ta₂O₅ present. Possibly this is caused by some fluorescence from metallic Ta which is illuminated by stray beam or from impurities in the sputtered layer. As explained in the section above, Ta in metallic Ta contributes more strongly to the XANES spectrum than Ta in Ta₂O₅ due to the higher density of Ta atoms per volume. The same effect accounts for the distorted ratio in point B.

A geological thin section as a typical application of spectromicroscopy using X-ray fluorescence contrast is used to further evaluate the effect of the order of the scanning axes in a practical application. Knowledge of the spatial distribution of oxidation states in geological material can provide crucial information about redox conditions and element speciation of infiltrating melts and fluids. The presented example is from an experimental study on fluid–rock interaction and the incorporation of As(III) and As(V) in apatite, which provides a tool to infer fluid composition and interaction conditions in ancient geological systems (Liu *et al.*, 2017). The sample in this study was prepared under special reaction conditions to study the uptake of As(III). For these measurements the beam size was approximately 0.5 μm × 0.5 μm, image pixel size 0.7 μm × 0.7 μm and the fixed-exit DCM was used. Due to the higher As concentration in comparison with the Ta test pattern, the dwell time per sampling interval could be reduced to 1 ms; a full XANES scan was thus completed within 0.2 s. Fig. 6 shows the large overview obtained by conventional scanning with the energy as the outer axis, with 85 energy points, while Fig. 6(a) is the grayscale concentration map of As. Fig. 6(b) shows the chemical phase map with the spatial distribution of the oxidation state obtained after fitting the XANES spectrum of each image pixel with a linear combination of As(III) and As(V). In this region of the sample, most of the As is present as As(III); only in the upper part of the scanned region the blue color indicates a mixture of As(III) and As(V).

A sub-region of this sample was scanned with the energy as the inner axis. Figs. 7(a) and 7(b) show the As intensity and two-dimensional fast XANES image of the region marked in Fig. 6(b). The As intensity map is shown in Fig. 7(a) while the chemical phase map with the distribution of the oxidation state is shown in Fig. 7(b). The data processing was the same as in the case for scanning the energy as the outer axis. The average (bulk) spectra acquired in continuous mode in comparison with the As(III) and As(V) standards, acquired as

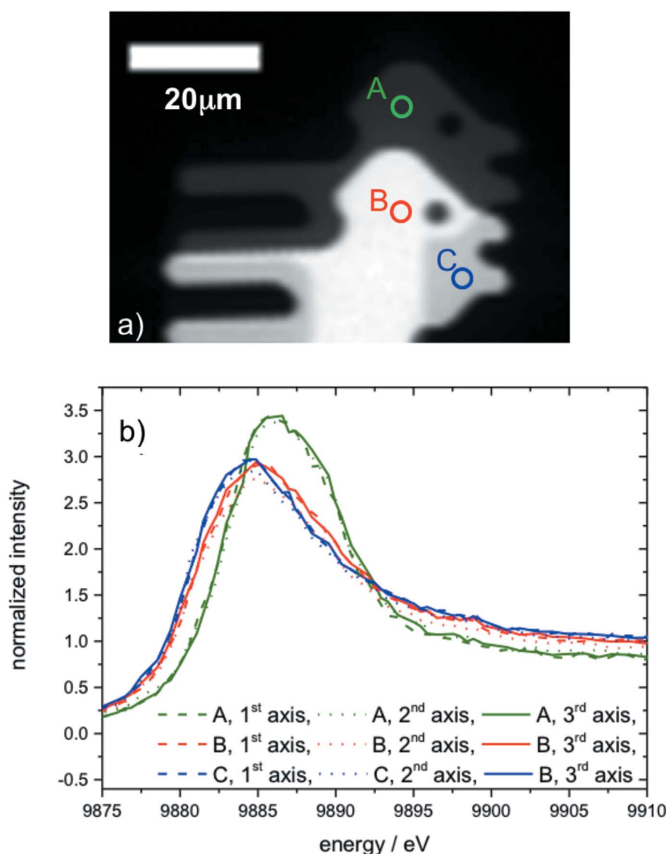


Figure 5
(a) Region of interest (scale bar is 20 μm) with selected points of interest for which the corresponding single-pixel XANES for each measurement scheme (energy axis) is plotted in (b).

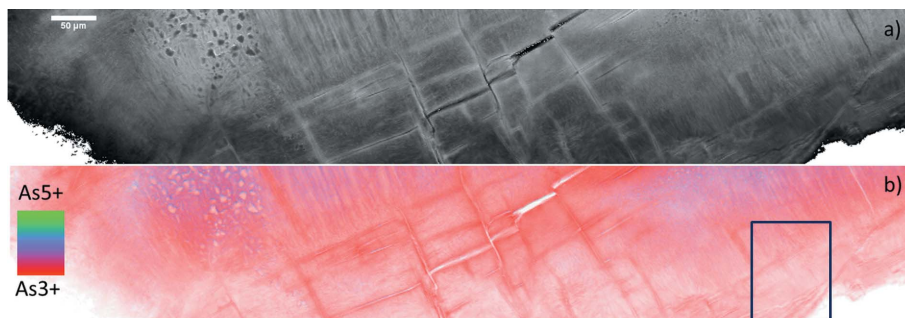


Figure 6

Large overview scan of a geological thin-section containing As-apatite with (a) the grayscale As concentration map and (b) the chemical phase map with the distribution of As(V) (green) and As(III) (red) with a 50:50 mixture (blue). The chemical phase map is derived from linear combination fitting of each single-pixel XANES with As(V) and As(III) references. The rectangular sub-region shows the area selected for further study (see Fig. 7).

a conventional energy stack, are shown in Fig. 7(c). Further geological context and the significance of the results on this sample are reported elsewhere (Liu *et al.*, 2017). The study with the specially prepared As-apatite samples revealed for the first time that As(III) can be incorporated into the apatite structure, although not as efficiently as As(V), and that As speciation is sensitive to the local fluid composition during crystallization.

A scan sequence with the Bragg angle as the inner axis is likely to be slowest overall due to the unnecessarily fine sampling of the energy in the pre- and post-edge regions, as the monochromator moves with a constant angular velocity (apart from the turnaround points), and delays at the turnaround points themselves. However, it shows superior spatial quality, and a modulated monochromator angular velocity (slowing near the edge) with improved turnaround delay could in principle be implemented. For scanning the energy as a middle or outer axis, the sampling in the pre- and post-edge region can be sparser without impacting the XANES quality and therefore reducing the overall acquisition time.

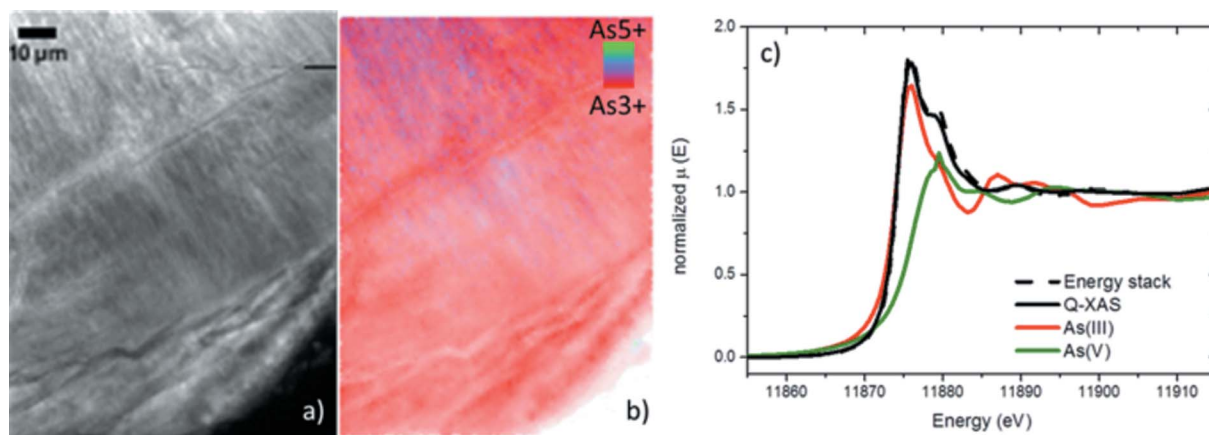


Figure 7

Selected sub-region of Fig. 6, scanned with the energy as the fastest axis. (a) As distribution map and (b) chemical phase map illustrating the distribution of the As oxidation state. (c) Average (bulk) spectra collected with the energy measured in the fast and slow dimension in comparison with the two references of As(III) and As(V).

4. Conclusions

A new fast XAS scanning method was recently implemented at the hard X-ray microprobe endstation P06, PETRA III, DESY, utilizing a Maia detector. Coordinated monochromator and undulator scanning in combination with the continuous readout of the hardware Bragg angle enabled acquisition of spectromicroscopy maps where each XANES spectra was acquired in 0.2 up to 30 s in fluorescence mode, depending on the concentration of the element of interest in the sample. We directly compared a region of interest measured with quick-XAS and conventional

mapping at multiple energies. The method was verified for two static samples where the XANES data show excellent agreement at the single-pixel level. The combination of improved spatial and temporal resolution may be necessary for rapidly changing samples, *e.g.* for following *in situ* chemical reactions or samples highly susceptible to beam damage where the rapid collection of single XANES spectra avoids issues with the emergence of chemical changes developing from latent damage.

Acknowledgements

The authors thank Weihua Liu for providing the geological sample. This research was carried out at the light source PETRA III at DESY, a member of the Helmholtz Association (HGF). We acknowledge travel funding provided by the International Synchrotron Access Program (ISAP) managed by the Australian Synchrotron, part of ANSTO, and funded by the Australian Government.

References

- Als-Nielsen, J., Grübel, G. & Clausen, B. S. (1995). *Nucl. Instrum. Methods Phys. Res. B*, **97**, 522–525.
- Boesenberg, U., Ryan, C. G., Kirkham, R., Siddons, D. P., Alfeld, M., Garrevoet, J., Núñez, T., Claussen, T., Kracht, T. & Falkenberg, G. (2016). *J. Synchrotron Rad.* **23**, 1550–1560.
- Chernikov, R., Welter, E., Caliebe, W., Wellenreuther, G. & Falkenberg, G. (2016). *J. Phys. Conf. Ser.* **712**, 012020.
- Frahm, R. (1988). *Nucl. Instrum. Methods Phys. Res. A*, **270**, 578–581.
- Frahm, R. (1989). *Rev. Sci. Instrum.* **60**, 2515–2518.
- Jonge, M. D. de, Ryan, C. G. & Jacobsen, C. J. (2014). *J. Synchrotron Rad.* **21**, 1031–1047.
- Khalid, S., Caliebe, W., Siddons, P., So, I., Clay, B., Lenhard, T., Hanson, J., Wang, Q., Frenkel, A. I., Marinkovic, N., Hould, N., Ginder-Vogel, M., Landrot, G. L., Sparks, D. L. & Ganjoo, A. (2010). *Rev. Sci. Instrum.* **81**, 015105.
- Kirkham, R., Dunn, P. A., Kuczewski, A. J., Siddons, D. P., Dodanwala, R., Moorhead, G. F., Ryan, C. G., De Geronimo, G., Beuttenmuller, R., Pinelli, D., Pfeffer, M., Davey, P., Jensen, M., Paterson, D. J., de Jonge, M. D., Howard, D. L., Küsel, M., McKinlay, J., Garrett, R., Gentle, I., Nugent, K. & Wilkins, S. (2010). *AIP Conf. Proc.* **1234**, 240–243.
- Liu, W., Mei, Y., Etschmann, B., Brugger, J., Pearce, M., Ryan, C. G., Borg, S., Wykes, J., Kappen, P., Paterson, D., Boesenberg, U., Garrevoet, J., Moorhead, G. & Falkenberg, G. (2017). *Geochim. Cosmochim. Acta*, **196**, 144–159.
- Liu, Y., Meirer, F., Wang, J., Requena, G., Williams, P., Nelson, J., Mehta, A., Andrews, J. C. & Pianetta, P. (2012). *Anal. Bioanal. Chem.* **404**, 1297–1301.
- Liu, Y., Meirer, F., Williams, P. A., Wang, J., Andrews, J. C. & Pianetta, P. (2012). *J. Synchrotron Rad.* **19**, 281–287.
- Mathon, O., Beteva, A., Borrel, J., Bugnazet, D., Gatla, S., Hino, R., Kantor, I., Mairs, T., Munoz, M., Pasternak, S., Perrin, F. & Pascarelli, S. (2015). *J. Synchrotron Rad.* **22**, 1548–1554.
- Meirer, F., Cabana, J., Liu, Y., Mehta, A., Andrews, J. C. & Pianetta, P. (2011). *J. Synchrotron Rad.* **18**, 773–781.
- Monico, L., Janssens, K., Hendriks, E., Vanmeert, F., Van der Snickt, G., Cotte, M., Falkenberg, G., Brunetti, B. G. & Miliani, C. (2015). *Angew. Chem. Int. Ed.* **54**, 13923–13927.
- Müller, O., Nachttegaal, M., Just, J., Lützenkirchen-Hecht, D. & Frahm, R. (2016). *J. Synchrotron Rad.* **23**, 260–266.
- Poswal, A. K., Agrawal, A., Poswal, H. K., Bhattacharyya, D., Jha, S. N. & Sahoo, N. K. (2016). *J. Synchrotron Rad.* **23**, 1518–1525.
- Prestipino, C., Mathon, O., Hino, R., Beteva, A. & Pascarelli, S. (2011). *J. Synchrotron Rad.* **18**, 176–182.
- Prieto, C., Lagarde, P., Dexpert, H., Briois, V., Villain, F. & Verdagner, M. (1992). *Meas. Sci. Technol.* **3**, 325–329.
- Ryan, C. G., Cousens, D. R., Sie, S. H., Griffin, W. L., Suter, G. F. & Clayton, E. (1990). *Nucl. Instrum. Methods Phys. Res. B*, **47**, 55–71.
- Ryan, C. G., Kirkham, R., Hough, R. M., Moorhead, G., Siddons, D. P., de Jonge, M. D., Paterson, D. J., De Geronimo, G., Howard, D. L. & Cleverley, J. S. (2010). *Nucl. Instrum. Methods Phys. Res. A*, **619**, 37–43.
- Ryan, C. G., Laird, J. S., Fisher, L. A., Kirkham, R. & Moorhead, G. F. (2015). *Nucl. Instrum. Methods Phys. Res. B*, **363**, 42–47.
- Ryan, C. G., Siddons, D. P., Kirkham, R., Li, Z. Y., de Jonge, M. D., Paterson, D. J., Kuczewski, A., Howard, D. L., Dunn, P. A., Falkenberg, G., Boesenberg, U., De Geronimo, G., Fisher, L., Halfpenny, A., Lintern, M. J., Lombi, E., Dyl, K. A., Jensen, M., Moorhead, G. F., Cleverley, J. S., Hough, R. M., Godel, B., Barnes, S. J., James, S. A., Spiers, K. M., Alfeld, M., Wellenreuther, G., Vukmanovic, Z. & Borg, S. (2014). *J. Phys. Conf. Ser.* **499**, 012002.
- Schroer, C. G., Kurapova, O., Patommel, J., Boye, P., Feldkamp, J., Lengeler, B., Burghammer, M., Riekel, C., Vincze, L., van der Hart, A. & Küchler, M. (2005). *Appl. Phys. Lett.* **87**, 124103.
- Siddons, D. P., Kirkham, R., Ryan, C. G., De Geronimo, G., Dragone, A., Kuczewski, A. J., Li, Z. Y., Carini, G. A., Pinelli, D. R., Beuttenmuller, R., Elliott, D., Pfeffer, M., Tyson, T. A., Moorhead, G. F. & Dunn, P. A. (2014). *J. Phys. Conf. Ser.* **499**, 012001.